Electronic Supplementary Material (ESI) for Journal of Materials Chemistry A.

Sustainable luminescent solar concentrators based on organic-inorganic hybrids modified by chlorophyll

A. R. Frias,[a,b] E. Pecoraro,[c] S.F.H. Correia,[a] L.M.G. Minas,[a,d] A.R. Bastos,[a,b] S. García-Revilla,[e] R. Balda,[e] S.J.L. Ribeiro,[c] P.S. André,[d] L.D. Carlos,[a] and R.A.S. Ferreira[a*]

[a]Department of Physics and CICECO – Aveiro Institute of Materials, University of Aveiro, 3810–193 Aveiro, Portugal; E-mail: rferreira@ua.pt
[b]Instituto de Telecomunicações, University of Aveiro, 3810–193 Aveiro, Portugal;
[c]UNESP - Institute of Chemistry, São Paulo State University, P.O. Box 355, 14801-970 Araraquara-SP, Brazil
[d]Department of Electric and Computer Engineering and Instituto de Telecomunicações, Instituto Superior Técnico, Universidade de Lisboa, 1049-001 Lisbon, Portugal
[e]Departamento de Física Aplicada I, Escuela de Ingeniería de Bilbao, Universidad del País Vasco UPV/EHU, Spain and Centro de Física de Materiales CSIC-UPV/EHU and Donostia International Physics Center, San Sebastián, Spain

---

Contents

Fig. S2. Dispersion curve of the refractive index for the (a) d-U(600) and (b) t-U(5000) based samples.

Fig. S3. XRD patterns of (a) d-U(600) based samples and (b) t-U(5000) based samples.

Fig. S4. ^{29}Si MAS NMR spectra of (a) dU6-chl-2 and (b) tU5-chl-1. The spectral fitting using a sum of Gaussian functions (shadowed areas) are ascribed to T^1, T^2, T^3 and Q silicon environments, and the overall fit (circles) is also shown.

Fig S5. ATR/FT-IR spectra for (a, c) d-U(600) and (b, d) t-U(5000) hybrids doped and undoped with chlorophyll extract, over different ranges.

Fig. S6. Absorption spectra of ethanolic solutions of chlorophyll with concentration values of 3×10^{16} (chl-1), 3×10^{17} (chl-2) and 3×10^{18} molecules.cm^{-3}(chl-3).

Fig. S7. Room temperature emission spectra of (a) dU6-chl-1, (b) dU6-chl-4, (c) tU5-chl-1 and (d) tU5-chl-4 excited in the blue region (410-435 nm).

Fig. S8. Emission spectra (11 K) of dU6-chl-3 and tU-chl-3.

Fig. S9. Room temperature absorption (purple dashed line) and emission spectra of (a) chl-2, (b) chl-3, (c) dU6-chl-2, (d) dU6-chl-3, (e) tU5-chl-2 and of (f) tU5-chl-3 excited at 415 nm.

Fig. S10. Room temperature excitation spectra monitored at different wavelengths for (a) tU5-chl-1, (b) dU6-chl-4, (c) tU5-chl-1 and (d) dU6-chl-4. The spectra for the ethanolic solutions (a,c) chl-1 [10^{-5} M] and (b,d) chl-4 [10^{-2} M] are also shown.

Fig. S11. Room temperature emission decay curves of (a) dU6-chl-1, (b) dU6-chl-3, (c) tU5-chl-1 and (d) tU5-chl-3 excited at 390 nm and monitored at 455 nm, 640 nm and 675 nm. The solid lines represent the best fit to the data (r2 >0.99) using a single exponential function. The respective residual plots are shown on the right-hand side.

Fig. S12. Temporal relative variation of the short-circuit current of dU6-chl-2.

Fig. S13. Simulated optical conversion efficiency determined by Monte Carlo ray-tracing, as function of the exposed area.

EXPERIMENTAL SECTION

Spectroscopic ellipsometry. The spectroscopic ellipsometry measurements were made using an AutoSE ellipsometer (HORIBA Scientific) with a total of 218 points in the wavelength interval 450-850 nm, an incidence angle (θ_0) of 69.8 °, and a signal to noise ratio of 25. A measurement spot area of 250×250 μm^2 was used. The refractive index values of the films were calculated assuming a two-layer structure model. The data were minimised using the Simplex algorithm. For the hybrids, the dispersion curves were determined using Cauchy absorbent model, given by:

$$n(\lambda) = A + \frac{B \cdot 10^4}{\lambda^2} + \frac{C \cdot 10^9}{\lambda^4} \tag{S1}$$

where n is the refractive index, λ is the wavelength (nm), and A, B and C are constants.

X-ray diffraction (XRD). XRD patterns were recorded using a Philips X'Pert MPD powder X-ray diffractometer. The samples were exposed to CuK_{α} radiation (1.54 Å) in a 2θ range between 1.00 and 70.0 ° with a step of 0.05 ° and time-acquisition of 40 s per step.

^{29}Si magic-angle spinning (MAS) NMR spectra. The ^{29}Si MAS NMR spectra were recorded with a Bruker III Avance 400 and Bruker III Avance 500 (9.4 T) spectrometer at 79.49 and 100.62 MHz, respectively. ^{29}Si MAS NMR spectra were recorded with 2 ls (ca. 30 °) rf pulses, a recycle delay of 60 s and at a 5.0 kHz spinning rate. ^{29}Si MAS NMR spectra were recorded with 2 μs (ca. 30 °) rf pulses, a recycle delay of 60 s and at a 5.0 kHz spinning rate.

Table S1. Thickness values of the films prepared by spin-coating on a glass substrate.

Designation	**Thickness (×10^{-6} m)**
d-U(600)	10.650
dU6-chl-2	11.200
dU6-chl-3	10.900
t-U(5000)	12.200
tU5-chl-2	13.500
tU5-chl-3	12.900

Table S2. Molar extinction coefficient (ε) at 665 nm for chlorophyll ethanolic solutions and chlorophyll-doped hybrids.

Designation	**ε (×10^4 $M^{-1}\cdot cm^{-1}$)**
chl-2	6.9
chl-3	6.9
dU6-chl-2	3.7
dU6-chl-3	5.7
tU5-chl-2	3.5
tU5-chl-3	4.7

Table S3. Typical values for the electrical power interval available at a USB port and required to charge small electronic devices. The number and size of dU6-chl-based LSCs needed are also indicated.

		Power (W)	LSCs A_s (m^2)*
PC USB		2.5	1.5×10^{-2}
devices	Mobile phone	5	3.0×10^{-2}
	Tablets	12	10^{-1}
	LED lamps	2.3 - 18	1.2×10^{-2}
	Movement sensors	0.32 - 0.45	2×10^{-3}
	Wi-fi routers	0.85-11	5×10^{-3}

*Estimated minimum surface area for a chl-based LSC (thickness of 1 cm) based on Monte-Carlo ray-tracing simulations.

Calculus of the optical conversion efficiency (η_{opt})

The η_{opt} can be described by weighting all the losses in the LSC, given by the product of several terms:[1]

$$\eta_{opt} = (1 - R)\eta_{abs}\eta_{SA}\eta_{yield}\eta_{Stokes}\eta_{trap}\eta_{mat} \tag{S2}$$

in which:

- $R=(1-n_i)^2/(1+n_i)^2$ is the Fresnel reflection coefficient for perpendicular incidence, in which n_i represents the refractive index of the emitting medium at the incident wavelength (λ_i).
- $\eta_{abs}=1-10^{-A}$ is the ratio of photons absorbed by the emitting layer to the number of photons falling on it, with A representing the absorbance value at λ_i.
- η_{SA} is the self-absorption efficiency, arising from self-absorption of the emitting centres, as detailed elsewhere.[2]
- η_{yield} is the emission quantum yield of the optically active centre at λ_i.
- $\eta_{Stokes}=\lambda_i/\lambda_p$, is the Stokes efficiency calculated by the energetic ratio between the average energy of the emitted photons and the incident energy.
- $\eta_{trap}=(1-1/n_p^2)^{1/2}$, the trapping efficiency, where n_p is the refractive index of the emitting medium at λ_p, is defined as the fraction of photons confined within the substrate.
- η_{tr} takes into account the transport losses due to matrix absorption and scattering, frequently it is considered that $\eta_{tr}=1$, as the transport and scattering losses are neglected.

As η_{opt} is dependent on the excitation wavelength, Eq. S2 must be modified taking into account the integration over the excitation spectrum limits (λ_1 and λ_2):

$$\eta_{opt} = \frac{1}{\lambda_2 - \lambda_1} \times \int_{\lambda_1}^{\lambda_2} (1 - R(\lambda))\eta_{abs}(\lambda)\eta_{yield}(\lambda)\eta_{Stokes}(\lambda)\eta_{trap}(\lambda)\,d\lambda \tag{S3}$$

yielding $\eta_{\mathrm{opt}}=2.4\%$.

Calculus of the experimental optical conversion efficiency (η_{opt}) and respective error ($\Delta\eta_{opt}$)

The experimental η_{opt} values were calculated through Eq. (1) in the manuscript. The associated error ($\Delta\eta_{opt}$) is given by:

$$(\Delta\eta_{opt})^2 = \left(\frac{\delta\eta_{opt}}{\delta I_{SC}^{L}}\Delta I_{SC}^{L}\right)^2 + \left(\frac{\delta\eta_{opt}}{\delta V_0^{L}}\Delta V_0^{L}\right)^2 + \left(\frac{\delta\eta_{opt}}{\delta A_e}\Delta A_e\right)^2 + \left(\frac{\delta\eta_{opt}}{\delta\eta_{solar}}\Delta\eta_{solar}\right)^2 + \left(\frac{\delta\eta_{opt}}{\delta A_s}\Delta A_s\right)^2 + \left(\frac{\delta\eta_{opt}}{\delta\eta_{LSC}}\Delta\eta_{LSC}\right)^2$$

$$\Leftrightarrow(\Delta\eta_{opt})^2 = \left(\frac{V_0^{L}A_e\eta_{Solar}}{I_{SC}V_0A_s\eta_{LSC}}\Delta I_{SC}^{L}\right)^2 + \Bigg(\frac{I_{SC}^{L}A_e\eta_{Solar}}{I_{SC}V_0A_s\eta_{LSC}}\Delta V$$
$$+ \left(-\frac{I_{SC}^{L}V_0^{L}A_e\eta_{Solar}}{(I_{SC})^2V_0A_s\eta_{LSC}}\Delta I_{SC}\right)^2 + \Bigg(-\frac{I_{SC}^{L}V_0^{L}}{I_{SC}(V_0}$$
$$+ \left(-\frac{I_{SC}^{L}V_0^{L}A_e\eta_{Solar}}{I_{SC}V_0(A_s)^2\eta_{LSC}}\Delta A_s\right)^2 + \Bigg(-\frac{I_{SC}^{L}V_0^{L}A}{I_{SC}V_0A_s} \qquad \text{(S4)}$$

where I_{SC}^{L} and V_0^{L} represent the short-circuit current and the open voltage when the PV device is coupled to the LSC, (I_{sc} and V_0 are the corresponding values of the PV device exposed directly to the solar radiation), A_s and A_e are the exposed and edge area respectively, η_{solar} is the efficiency of the PV device relatively to the total solar spectrum and η_{PV} is the efficiency of the PV device at the LSC emission wavelengths. The errors associated with each variable were considered as follows: $\Delta I_{SC}^{L} = \Delta I_{SC} = 10^{-10}$ A is the current experimental uncertainty, $\Delta V_0^{L} = \Delta V_0 = 10^{-3}$ V is the voltage experimental uncertainty, $\Delta A_e = \Delta A_s = 10^{-7}$ m^2 is experimental uncertainty associated with the area and $\Delta\eta_{solar} = \Delta\eta_{LSC} = 10^{-2}$ is the photodiode experimental uncertainty.

Spectroscopic ellipsometry

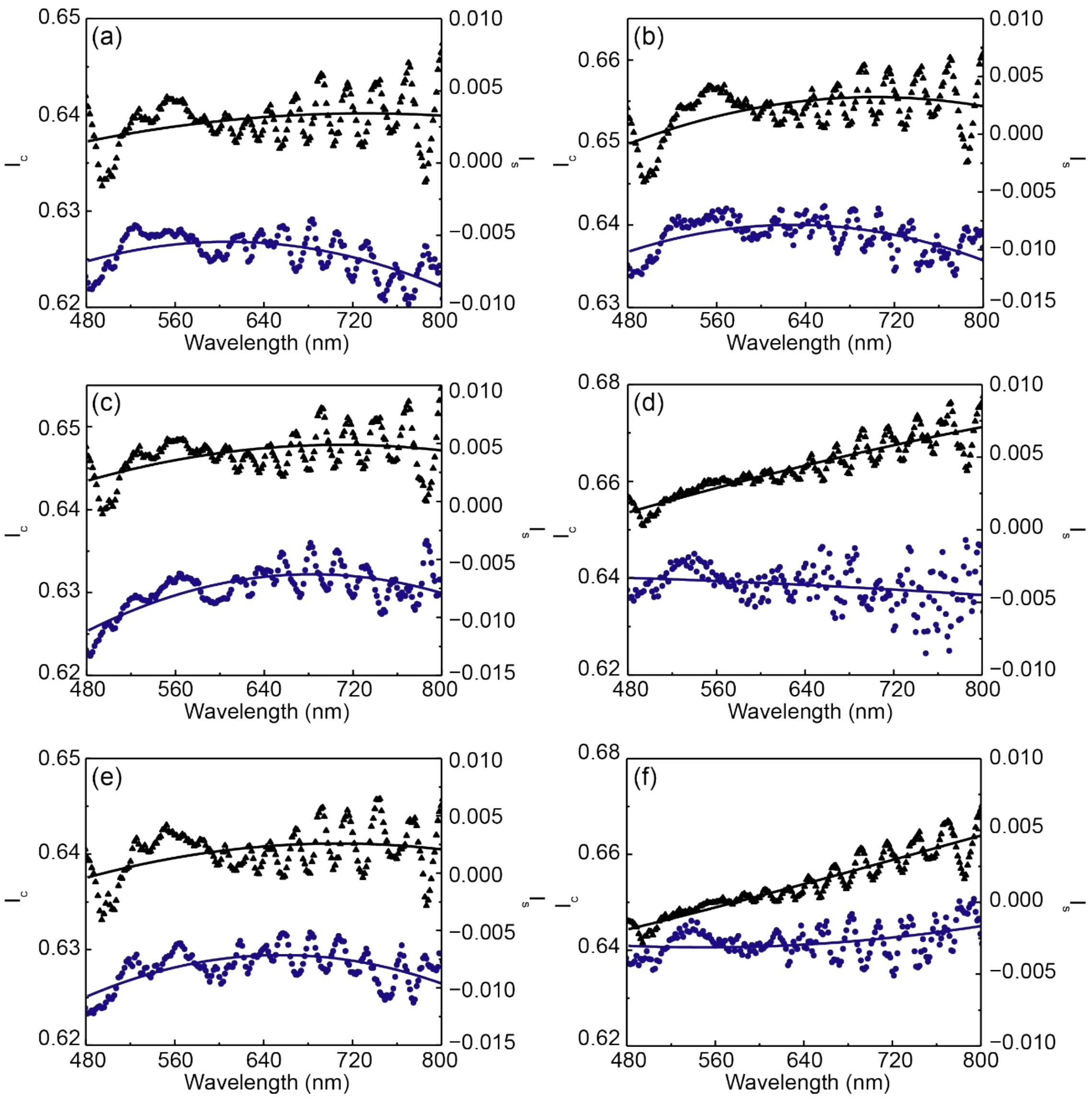

Fig. S1. Ellipsometric parameters Ic (black triangles) and Is (blue circles) measured for the active layer of (a) d-U(600), (b) t-U5000, (c) dU6-chl-2, (d) tU5-chl-2, (e) dU6-chl-3, (f) tU5-chl-3; the lines represent the best data fit (r^2>0.9).

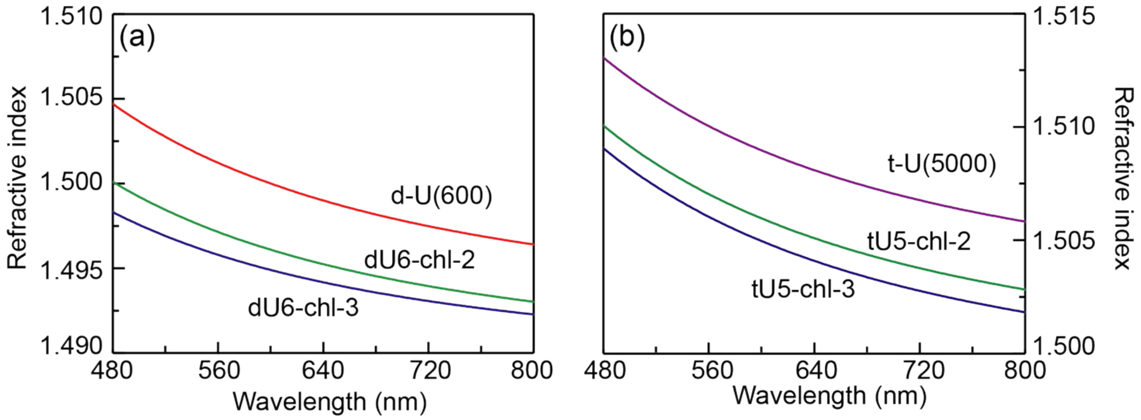

Fig. S2. Dispersion curve of the refractive index for the (a) d-U(600) and (b) t-U(5000) based samples.

The trapping efficiency can be calculated from the dispersion curve data in Fig. S2, using the following expression:

$$\eta_{trap} = \sqrt{\left(1 - \frac{1}{n_p^2}\right)} \qquad \text{(S5)}$$

where n_p is the refractive index of the emitting medium at the emission wavelength (in this case, 670 nm) could be estimated. This parameter determines the fraction of photons confined within the substrate, accounting for the emission losses at the surface through a so-called escape cone with an aperture angle $\theta_c = 2 \times \sin^{-1}\left(1/n_p\right)$. According to the refractive index dispersion curves, η_{trap} ~75% for all the hybrids.

X-ray diffraction

XRD patterns were recorded using a Philips X'Pert MPD powder X-ray diffractometer. The samples were exposed to CuKα radiation (1.54 Å) in a 2h range between 1.00 and 70.00° with a step of 0.05 and time-acquisition of 40 s per step.

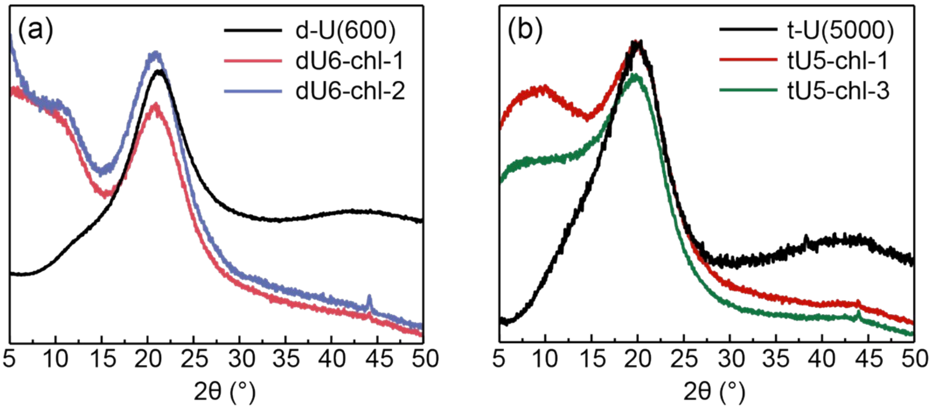

Fig. S3. XRD patterns of (a) d-U(600)- and (b) t-U(5000)-based hybrids.

The XRD patterns of the chlorophyll-related hybrids are analogous to that of the isolated d-U(600) [3] and t-U(5000) [4] hosts. The patterns show a broad band centerd at 21.20° and 20°, respectively, associated with the presence of amorphous siliceous domains [5,6]. The second order of these bands appears as an even broader weak hump around 39-44° [7]. Additionally, between 12 and 14° a shoulder is clearly discerned in all patterns. This feature has been ascribed to other intra-siloxane domains in-plane ordering with a characteristic distance of ca. 7.0 Å. For the d-U(600) based hybrids a characteristics distance of d=4.2±0.2 Å and for the t-U(5000) based hybrids a distance of d=4.4±0.2 Å were estimated using the Bragg law [3,4]. The fact that there are no significant changes in the patterns after incorporating the chlorophyll, suggests that the local structure of the hybrid host remains essentially unaltered.

^{29}Si Nuclear Magnetic Resonance

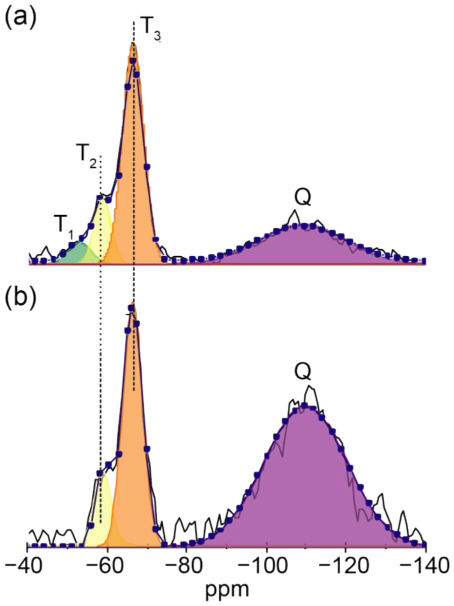

Fig. S4. ^{29}Si MAS NMR spectra of (a) dU6-chl-2 and (b) tU5-chl-1. The spectral fitting using a sum of Gaussian functions (shadowed areas) are ascribed to T^1, T^2, T^3 and Q silicon environments, and the overall fit (circles) is also shown.

The ^{29}Si MAS NMR spectra of tU5-chl-1 and dU6-chl-2 are very similar being dominated by characteristic peaks at –60.5 and –65.4 ppm, assigned to the $CH_2Si(OSi)_2(OR)$ (T^2) and $CH_2Si(OSi)_3$ (T^3) silicon environments [4,8,9]. For the d-U(600)-based hybrids another low-intensity peak at –57.6 from the $CH_2Si(OSi)(OR)_2$ (T^1) local sites is also discerned. The signals between *ca.* –90 and –130 ppm are assigned to $(\equiv SiO)_2Si(OH)_2$ (Q^2, geminal silanols), $(\equiv SiO)_3SiOH$ (Q^3, single silanol) and $(\equiv SiO)_4Si$ (Q^4, siloxane) local environments indicating the pre-hydrolysis of the t-UPTES(5000) and d-UPTES(600) precursor, respectively [10].

FT-IR spectroscopy

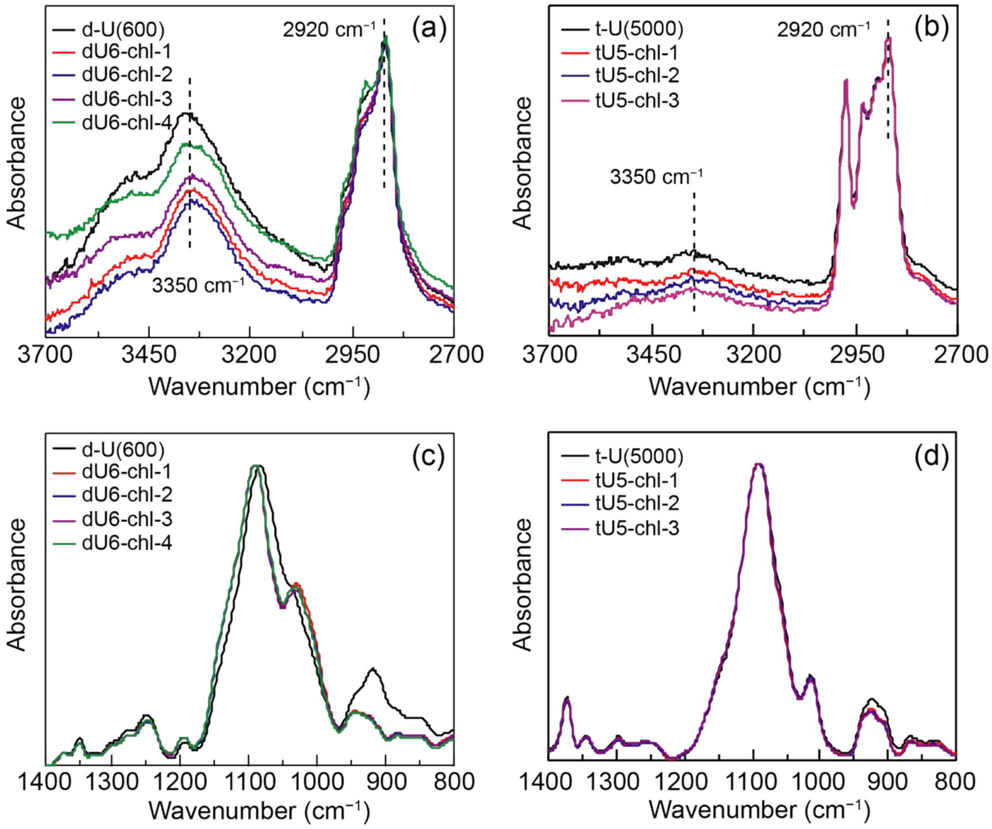

Fig S5. ATR/FT-IR spectra for (a, c) d-U(600) and (b, d) t-U(5000) hybrids doped and undoped with chlorophyll extract, over different ranges.

Figure S4 (a,b) shows the ATR/FT-IR spectra for selected chlorophyll-based hybrids and those of the undoped d-U(600) [11] and t-U(5000) [4] are also presented to render easier the analysis. Range (a,b) includes ν_{NH} hydrogen-bonded amide II ×2 (3350 cm^{-1}), ν_aCH_3 (2965 cm^{-1}), ν_aCH_2 (2920 cm^{-1}) and ν_{sCH3} (2870 cm^{-1}); range (c,d) includes transitions associated to ketone, propionate and carbomethoxy $\nu_{C=O}$ (1712 cm^{-1}) from chlorophyll and pheophytin, $\nu C=O$ amide I (1637 cm^{-1}), δNH amide II (1560 cm^{-1}), δCH_2, δCH_3 (1453 cm^{-1}) and δ_{CH} from phytol (1470-1460 cm^{-1} - C_{20} hydrocarbon tail from chlorophyll and pheophytin) [12]. Figure S4 (c,d) includes transitions associated mainly to PEO chain, such as 1350 cm^{-1} (ω_{CH2}), 1250-1195 cm^{-1} (τ_{CH2}); siliceous nanodomains, 1083 cm^{-1} (ν_{CO}, ν_{SiOSi} for SiO_2 clusters) and polar groups attached to the chlorin ring of chlorophyll and pheophytin, 1031 cm^{-1} (ν_{CO} and ν_{COCH3}) and 918 cm^{-1} (ν_{CC} and ρ_{CH2}). The analysis of the range (a,b) shows that the t-U(5000) host presents very low hydrogen bonding interactions for amide II groups, once the relative intensity of the peak at 3350

cm^{-1} to the group of peaks centered at ~2920 cm^{-1} (corresponding to vibrations of CH_2 and CH_3 PEO groups) is much lower than for the d-U(600) host. Person *et al.* [13] have demonstrated that the reduction in intensity of this mode (and sometimes also in frequency), may be correlated with a decrease in hydrogen-bonding strength. This would imply that the hydrogen bonds in t-U(5000) are weaker than in d-U(600). It seems such feature is correlated to the length of the PEO chain [11].

UV-Vis absorption spectroscopy

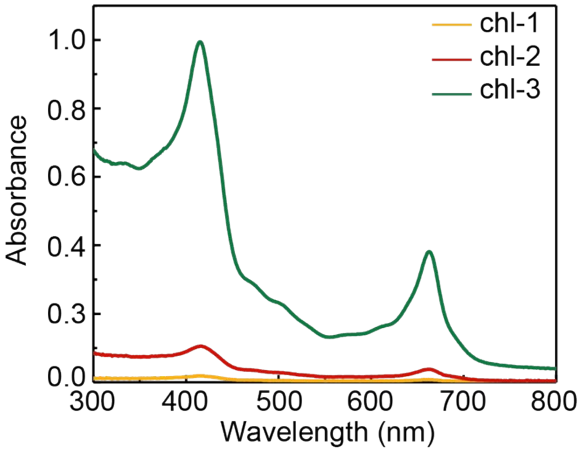

Fig. S6. Absorption spectra of ethanolic solutions of chlorophyll with concentration values of 3×10^{16} (chl-1), 3×10^{17} (chl-2) and 3×10^{18} molecules.cm^{-3}(chl-3).

Photoluminescence spectroscopy

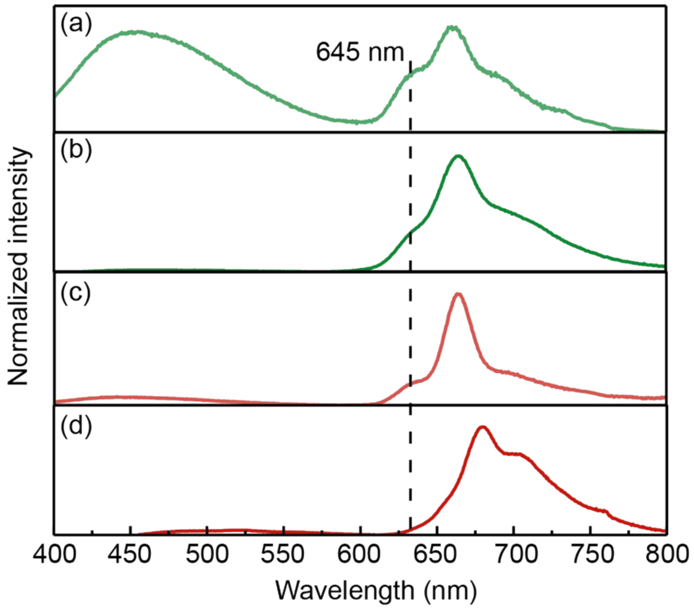

Fig. S7. Room temperature emission spectra of (a) dU6-chl-1, (b) dU6-chl-4, (c) tU5-chl-1 and (d) tU5-chl-4 excited in the blue region (410-435 nm).

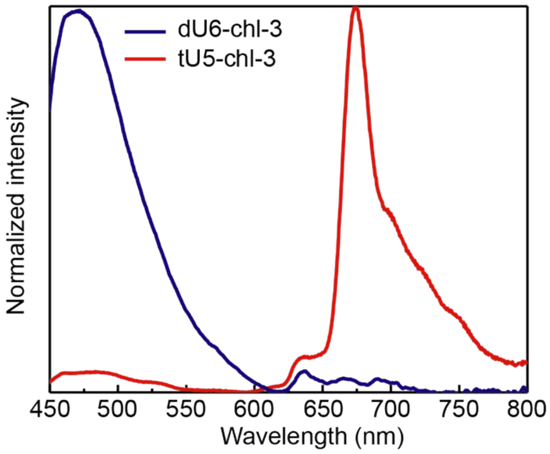

Fig. S8. Emission spectra (11 K) of dU6-chl-3 and tU-chl-3.

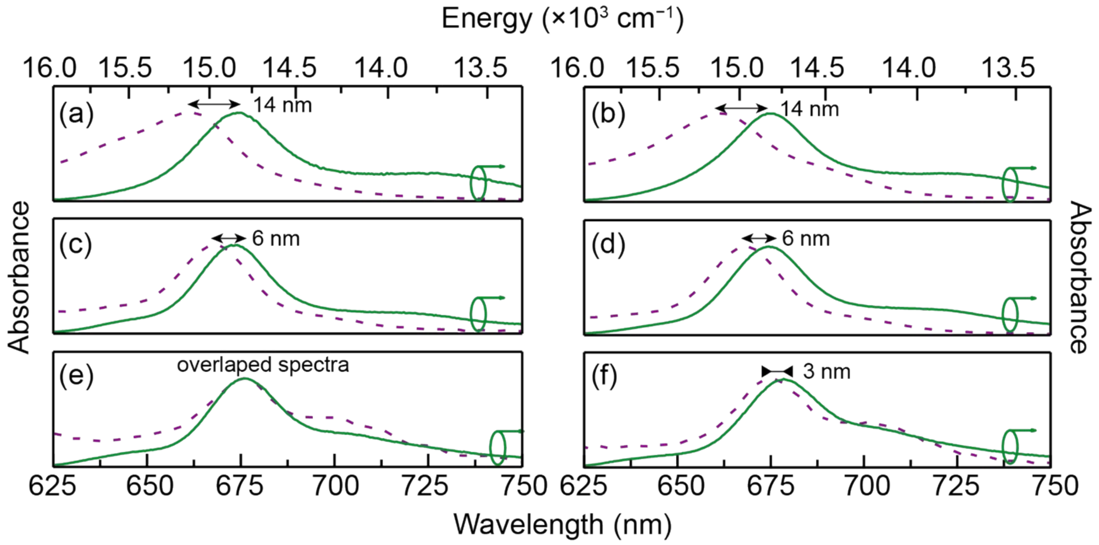

Fig. S9. Room temperature absorption (purple dashed line) and emission spectra of (a) chl-2, (b) chl-3, (c) dU6-chl-2, (d) dU6-chl-3, (e) tU5-chl-2 and of (f) tU5-chl-3 excited at 415 nm.

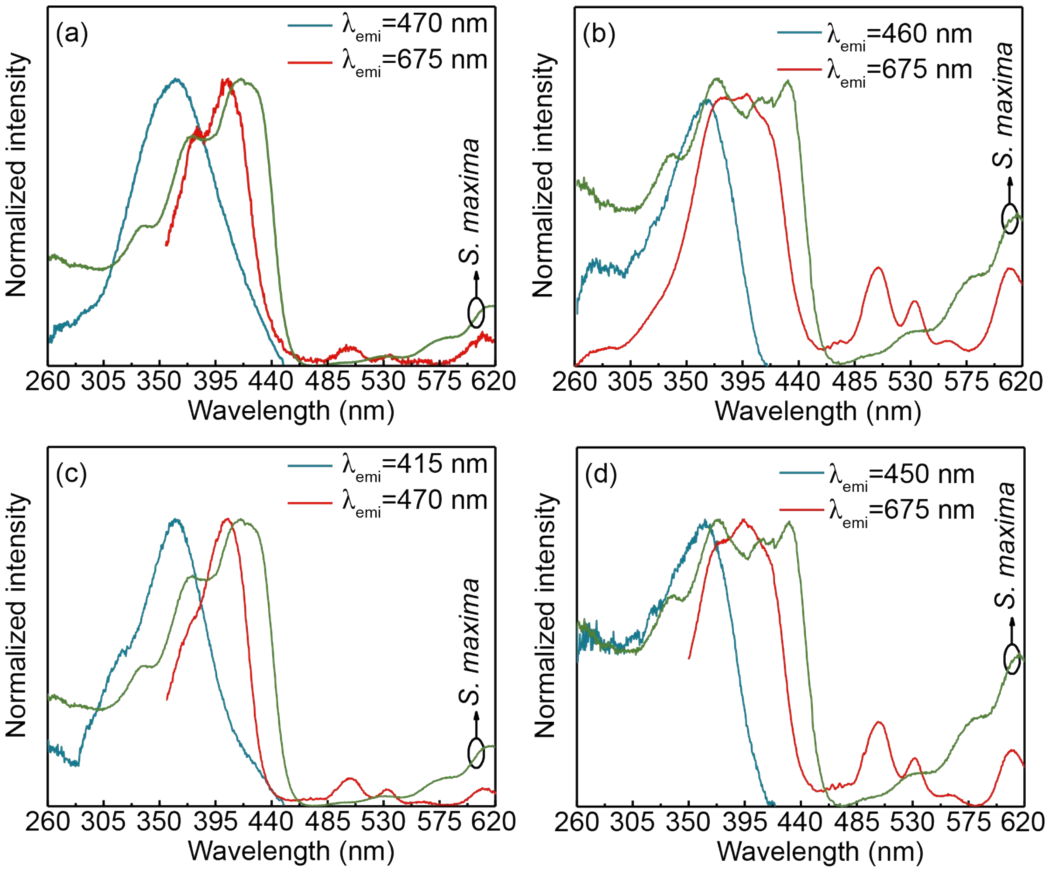

Fig. S10. Room temperature excitation spectra monitored at different wavelengths for (a) tU5-chl-1, (b) dU6-chl-4, (c) tU5-chl-1 and (d) dU6-chl-4. The spectra for the ethanolic solutions (a,c) chl-1 [10^{-5} M] and (b,d) chl-4 [10^{-2} M] are also shown.

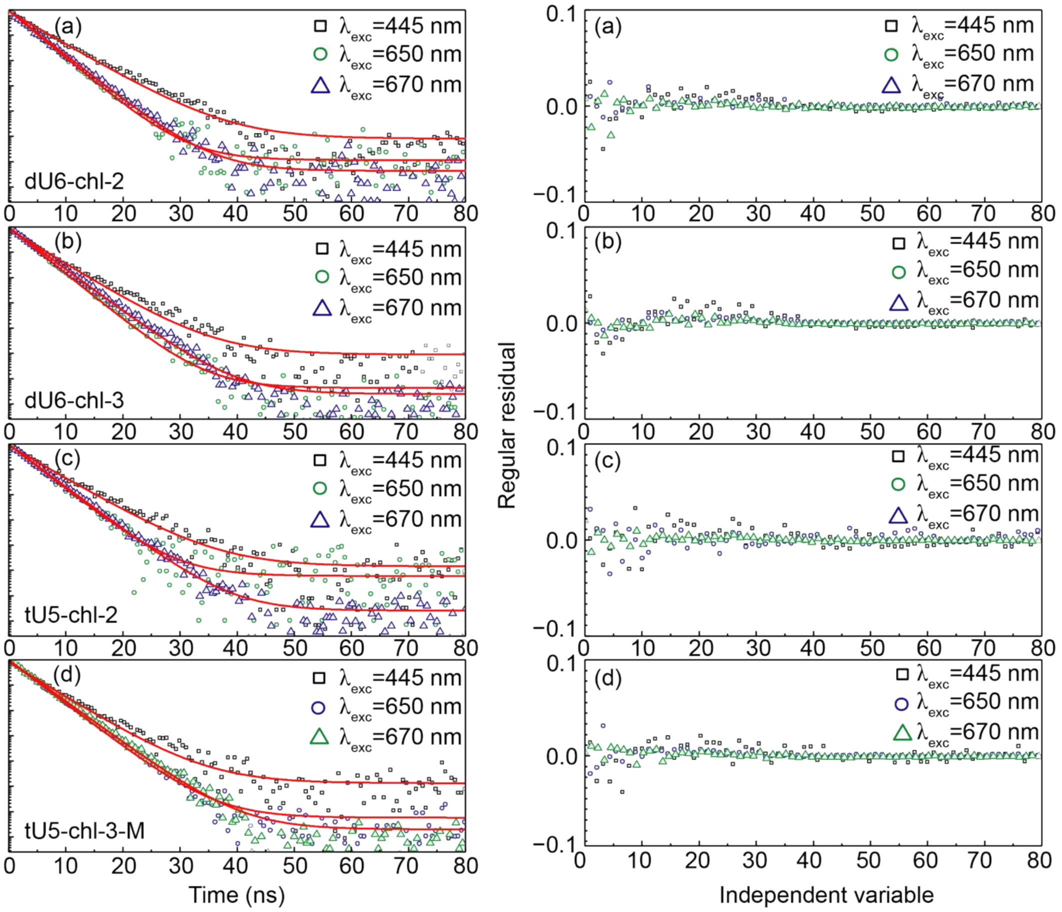

Fig. S11. Room temperature emission decay curves of (a) dU6-chl-1, (b) dU6-chl-3, (c) tU5-chl-1 and (d) tU5-chl-3 excited at 390 nm and monitored at 455 nm, 640 nm and 675 nm. The solid lines represent the best fit to the data (r^2 >0.99) using a single exponential function. The respective residual plots are shown on the right-hand side.

Photo-stability under AM1.5 illumination

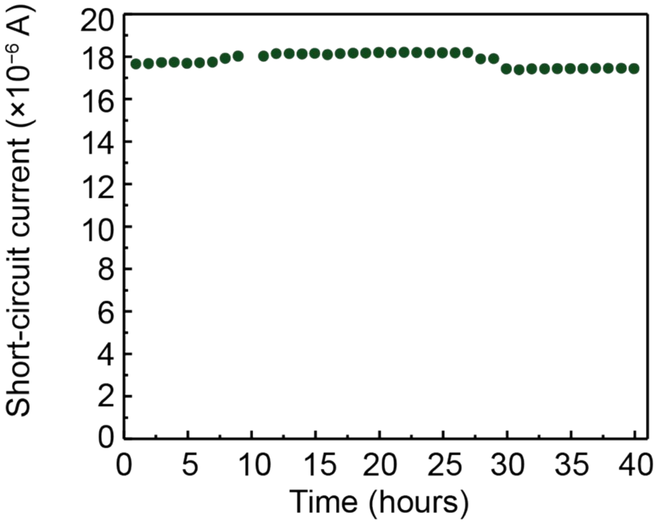

Fig. S12. Temporal relative variation of the short-circuit current of dU6-chl-2.

Monte Carlo ray-tracing modelling

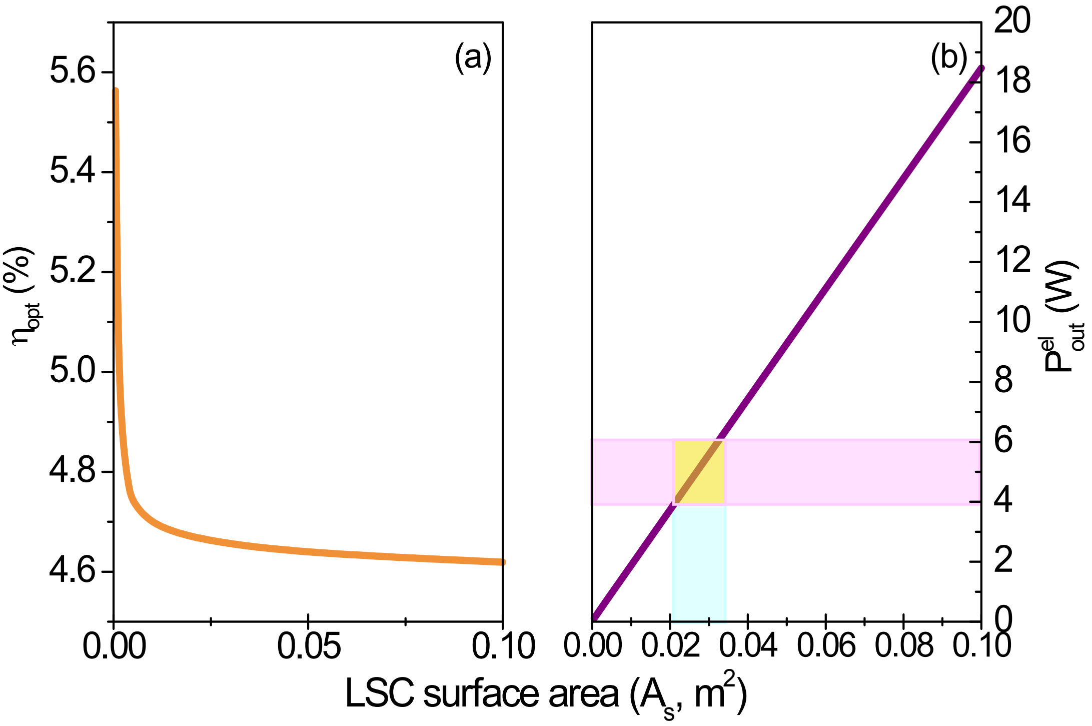

Fig. S13. (a) Monte Carlo ray-tracing optical conversion efficiency as function of the LSC surface area and (b) predicted output electrical power (the shadow area highlight the power vs surface required for low-voltage devices).

References

1. T. Dienel, C. Bauer, I. Dolamic and D. Bruhwiler, *Sol. Energy*, 2010, **84**, 1366.
2. Z. Krumer, W. G. J. H. M. van Sark, R. E. I. Schropp and C. D. Donega, *Sol. Energ. Mat. Sol. C.*, 2017, **167**, 133.
3. L. S. Fu, R. A. S. Ferreira, N. J. O. Silva, L. D. Carlos, V. D. Bermudez and J. Rocha, *Chem Mater*, 2004, **16**, 1507.
4. V. T. Freitas, P. P. Lima, R. A. S. Ferreira, E. Pecoraro, M. Fernandes, V. D. Bermudez and L. D. Carlos, *J. Sol-Gel Sci. Technol.*, 2013, **65**, 83.
5. A. R. West, *Solid state chemistry and its applications*, John Wiley & Sons, 2007.
6. C. Giacovazzo, H. L. Monaco, D. Viterbo, F. Scordari, G. Gilli, G. Zanotti and M. Catti, *Fundamentals of Crystallography*, Oxford Science Publications: New York, 1995.
7. P. P. Lima, S. S. Nobre, R. O. Freire, S. A. Junior, R. A. S. Ferreira, U. Pischel, O. L. Malta and L. D. Carlos, *J. Phys. Chem. C*, 2007, **111**, 17627.
8. V. T. Freitas, P. P. Lima, V. D. Bermudez, R. A. S. Ferreira and L. D. Carlos, *Eur. J. Inorg. Chem.*, 2012, 10.1002/ejic.201200823, 5390.
9. L. D. Carlos, R. A. S. Ferreira, I. Orion, V. D. Bermudez and J. Rocha, 2000, **87-9**, 702.
10. L. S. Fu, R. A. S. Ferreira, A. Valente, J. Rocha and L. D. Carlos, *Micropor. Mesopor. Mat.*, 2006, **94**, 185.
11. V. D. Bermudez, L. D. Carlos and L. Alcacer, *Chem Mater*, 1999, **11**, 569.
12. A. S. Holt and E. E. Jacobs, *Plant Physiol*, 1955, **30**, 533.
13. W. B. Person and G. Zerbi, *Vibrational intensities in infrared and Raman spectroscopy* Elsevier Science Ltd., 1982.